ARTICLE

Subsurface imaging based on polarization analysis of microtremor Rayleigh waves

Qingling Du[1,2]*, Qian Xu[1], Nan Guo[3], Shuai Liu[1], Shijie Liu[4], and Denghui Gao[1]

[1]College of Civil Engineering and Architecture, Huanghuai University, Zhumadian, Henan, China

[2]Henan International Joint Laboratory of Structural Mechanics and Computational Simulation, Huanghuai University, Zhumadian, Henan, China

[3]School of Civil and Hydraulic Engineering, Lanzhou University of Technology, Lanzhou, Gansu, China

[4]Department of Architecture and Civil Engineering, Lvliang University, Lvliang, Shanxi, China

*Corresponding author:
Qingling Du
duqingling@huanghuai.edu.cn

Abstract

The precise identification of adverse geological bodies, such as goafs, karst cavities, and faults, is crucial for engineering safety and economic viability. However, conventional drilling methods suffer from high costs, limited coverage, and the risk of overlooking anomalies. While existing geophysical techniques can address drilling's limitations, they are often constrained by non-uniqueness and insufficient resolution. To address these challenges, this paper proposes a novel technique for stratigraphic evaluation based on the polarization analysis of microtremor surface waves, aiming to improve the accuracy and efficiency of identifying dynamic site parameters in complex geological settings. We systematically validated the feasibility of using the elliptical polarization ratio of Rayleigh waves for subsurface characterization through theoretical analysis and field data. Numerical simulations confirmed that the method can clearly identify localized geological anomalies under noise-free conditions. For field data processing, we developed a workflow to extract Rayleigh waves with a high signal-to-noise ratio from microtremors. This workflow isolates valid wave components using principal frequency filtering and directional discrimination, while mitigating noise impact on dispersion estimation. The final polarization ratio profile strongly correlated with magnetotelluric resistivity data, successfully imaging goafs, fractured zones, and bedrock interfaces. Stacking codirectional wave events further enhanced deep structural resolution and resulted in consistency. In conclusion, this study demonstrates that the polarization-based method is a feasible, flexible, and promising tool for engineering applications, offering a reliable foundation for fine-scale site characterization.

1. Introduction

With the rapid advancement of urbanization and infrastructure construction, the influence of site geological conditions on project safety and economy has become increasingly significant. The precise identification of adverse geological bodies with strong

lateral heterogeneity, such as goafs, karst caves, and fault fracture zones, has emerged as a core task in engineering investigation.[1] This demand for site characterization is particularly urgent in areas with complex geological conditions, driven by the accelerated pace of development and the continuous expansion of underground space utilization. Conventional borehole-based investigation methods, however, exhibit pronounced limitations. While capable of providing local point-based geological information, they are prohibitively expensive, suffer from low sampling density and limited resolution, and are ill-suited for large-scale continuous detection. Consequently, they are prone to overlooking geological anomalies between boreholes, failing to meet the requirements of fine-scale investigation for modern large-scale engineering projects.[2] To compensate for these deficiencies, geophysical methods, including high-density resistivity, seismic reflection, and magnetotelluric methods, have been widely employed.[3-5] Nevertheless, these techniques are often hampered by issues such as non-uniqueness of solutions, signal interference, and inadequate resolution, which restrict their reliability and precision in complex geological settings. Therefore, the development of efficient, high-precision, low-cost, and adaptable multiparameter geophysical exploration technologies has become a critical direction for enhancing the capability of site geological structure evaluation.

Surface wave exploration techniques, by virtue of their advantages—such as high sensitivity to vertical stratigraphic changes, a broad depth of investigation, and ease of field implementation—have been extensively applied in the identification of site dynamic parameters and the inversion of subsurface structures.[6] In particular, Rayleigh waves, as the principal type of surface wave, possess propagation characteristics that are closely correlated with the elastic parameters of the ground (*e.g.*, shear wave velocity and Poisson's ratio). Consequently, analyzing the dispersion characteristics of Rayleigh waves has become a mainstream method for subsurface structure inversion.[7,8] However, traditional Rayleigh wave dispersion analysis methods predominantly rely on active seismic sources. In complex sites, such as densely populated urban areas or mountainous terrain, these methods are susceptible to interference from environmental noise, which degrades the accuracy of extracted dispersion curves. Furthermore, the deployment of active sources constrains both the investigation range and operational flexibility. In contrast, microtremor exploration utilizes natural environmental vibrations (*e.g.*, from traffic, wind loads, and crustal micro-movements) as its energy source. Requiring no artificial excitation, this approach offers significant advantages, including being non-destructive,

enabling large-scale surveys, and adapting to complex site conditions. It thus presents a new paradigm for overcoming the application bottlenecks of traditional surface wave exploration techniques.[9-11]

Microtremor signals are rich in surface wave information, particularly Rayleigh wave components, whose propagation characteristics can also reflect the vertical stratification and lateral heterogeneity of strata. Early research on microtremor surface waves primarily concentrated on the extraction and inversion of dispersion curves. By utilizing the power spectral density or cross-correlation function of microtremor signals, these methods obtain Rayleigh wave dispersion characteristics to subsequently invert the shear wave velocity structure of the strata.[12-15] However, when applied to laterally heterogeneous sites—such as those with local geological anomalies such as goafs and fractured zones—these methods face limitations. Due to their neglect of the polarization characteristics of Rayleigh waves, they struggle to accurately identify the spatial location and morphological features of such anomalies, leading to reduced reliability of the inversion results. Rayleigh waves exhibit unique elliptical polarization characteristics during propagation. Their elliptical polarization ratio (the ratio of the major to minor axis) is not only correlated with the elastic parameters of the strata but is also highly sensitive to lateral heterogeneity. This characteristic provides a key technological breakthrough for achieving fine-scale structural evaluation of complex sites.[16]

Recent years have witnessed a surge in research on Rayleigh wave polarization analysis. Theoretical investigations have established its utility, starting with the joint inversion method by Arai and Tokimatsu that enhanced Vs-profile accuracy.[17] Subsequent studies by Woodhouse and Maupin confirmed that Rayleigh wave ellipticity can constrain the non-uniqueness of dispersion inversion.[18-21] The link between the H/V spectral ratio and Rayleigh wave ellipticity was further solidified in other works.[22,23] Numerical simulations by Yu and Liu[24] revealed that the polarization dispersion method offers superior sensitivity and lateral resolution compared to conventional velocity dispersion, particularly in laterally inhomogeneous media. The method's versatility is evidenced by its successful application in diverse fields, including depth calibration,[25] sedimentary layer thickness estimation,[26] polar ice sheet investigation,[27] and archaeological surveys.[28]

Nevertheless, a fundamental challenge persists: The extraction of Rayleigh wave polarization with a high signal-to-noise ratio (SNR) from the complex ambient microtremor field. This field is a superposition of multiple wavefields—including multidirectional Rayleigh waves,

Love waves, body waves, and background noise—which degrades polarization estimation accuracy.[29] In response, two primary technical pathways have emerged. The first involves array-based wavefield separation, which leverages the spatial characteristics of waves to isolate Rayleigh waves.[30] The second pathway focuses on transient event screening, utilizing time-frequency analysis and machine learning to select high-SNR events, such as distant earthquakes or industrial vibrations that provide a pristine signal for polarization analysis.[31,32]

Consequently, engineering site evaluation currently faces a confluence of challenges: Significant constraints from conventional methods, strong non-uniqueness in geophysical inversion, and the formidable task of extracting polarized signals from microtremors. To address these gaps, this research centers on the elliptical polarization of Rayleigh waves, with a core focus on resolving the extraction of high-SNR polarization signals under complex site conditions. Through an optimized data processing scheme, this work seeks to improve the precision for detecting subsurface adverse geological structures, thereby offering a more robust technological foundation for site characterization.

2. Methods

Within a homogeneous medium, a strong correlation exists between the ellipticity of Rayleigh surface waves and the Poisson's ratio of the constituent material. Given that Poisson's ratio is a vital parameter in the characterization of subsurface geological structures, this section is dedicated to theoretically elucidating how wave ellipticity can be employed as a significant indicator for site evaluation.

For the theoretical analysis, we consider waves propagating in an infinite, homogeneous medium, where the fundamental form of the wave equation solution is $e^{jk(x-Vt)}$. The motion trajectory of a particle is defined by its radial displacement component u and its vertical displacement component w. Through the established relationship between displacement and potential functions, the corresponding potentials can be determined. Consequently, the formulas for the particle's radial and vertical displacements can be derived as:

$$\begin{cases} u = A(-e^{-mkz} + \dfrac{2mn}{n^2+1}e^{-nkz})ike^{i(\omega t - kx)} \\ w = A(-me^{-mkz} + \dfrac{2mn}{n^2+1}e^{-nkz})ke^{i(\omega t - kx)} \end{cases} \quad (1)$$

In this expression, m and n represent the attenuation coefficients, whereas A denotes the energy coefficient. The analytical expressions for the vertical and horizontal

components of displacement are derived by applying Euler's transformation to the equation and extracting its real part.

$$\begin{cases} u = A\left(e^{-mkz} - \dfrac{2mn}{n^2+1}e^{-nkz}\right)ksin(\omega t - kx) \\ w = A(-me^{-mkz} + \dfrac{2mn}{n^2+1}e^{-nkz})kcos(\omega t - kx) \end{cases} \quad (2)$$

Based on **Equation 2**, the displacement of Rayleigh waves in a homogeneous half-space was calculated for various Poisson's ratios. The variation of this displacement with depth, normalized by the half-wavelength, was subsequently characterized. The results demonstrate that the energy of Rayleigh waves attenuates exponentially with depth and is predominantly confined within a depth range of one wavelength. Furthermore, the variation in Poisson's ratio was found to only marginally affect the rate of this energy attenuation.[24]

In addition, **Equation 2** reveals that for Rayleigh waves propagating along the free surface of a homogeneous elastic half-space, the two displacement components satisfy an elliptical equation:

$$\left(\frac{u}{a}\right)^2 + \left(\frac{w}{b}\right)^2 = 1 \quad (3)$$

where $a = Ak\left(e^{-mkz} - \dfrac{2mn}{n^2+1}e^{-nkz}\right)$ and $b = Ak\left(-me^{-mkz} + \dfrac{2mn}{n^2+1}e^{-nkz}\right)$ are the semi-major and semi-minor axes of the ellipse, respectively. This demonstrates that the particle motion trajectory of a Rayleigh wave is elliptical. Based on this elliptical trajectory, the ellipticity $E(z)$ can be defined as the ratio of the amplitudes of the horizontal and vertical displacement components:

$$E(z) = \left| \frac{e^{-mkz} - \dfrac{2mn}{n^2+1}e^{-nkz}}{-me^{-mkz} + \dfrac{2mn}{n^2+1}e^{-nkz}} \right| \quad (4)$$

At the free surface ($z = 0$), the ellipticity is given by:

$$E(0) = \frac{n^2+1-2mn}{m(1-n^2)} \quad (5)$$

The relationship between the Rayleigh wave velocity, S-wave velocity, P-wave velocity, and Poisson's ratio is as follows:

$$\frac{V_R}{\beta} = \frac{0.87 + 1.12\sigma}{1+\sigma} \quad (6)$$

$$\frac{V_R}{\alpha} = \frac{(0.87 + 1.12\alpha)\sqrt{(1 - 2\tilde{A})\,/\,2(1 - \alpha)}}{1 + \alpha} \tag{7}$$

The following equations are obtained by substituting the solutions for the P- and S-wave potential functions into their respective governing equations:

$$m^2 = 1 - \frac{V_R^2}{\alpha^2},\; n^2 = 1 - \frac{V_R^2}{\beta^2} \tag{8}$$

In a homogeneous half-space, the parameters m and n are constants, and consequently, the ellipticity of Rayleigh waves is also a constant. By combining **Equations 6, 7**, and **8**, it is evident that *m* and *n* are dependent solely on Poisson's ratio of the homogeneous half-space. Thus, **Equation 5** can be reformulated as:

$$E = \frac{2 - \left(\dfrac{0.87 + 1.12\sigma}{1 + \sigma}\right)^2 - 2\sqrt{\left[1 - \dfrac{(0.87 + 1.12\sigma)^2(1 - 2\sigma)}{2(1 + \sigma)^2(1 - \sigma)}\right]\left[1 - \left(\dfrac{0.87 + 1.12\sigma}{1 + \sigma}\right)^2\right]}}{\left(\dfrac{0.87 + 1.12\sigma}{1 + \sigma}\right)^2 \sqrt{1 - \dfrac{(0.87 + 1.12\sigma)^2(1 - 2\sigma)}{2(1 + \sigma)^2(1 - \sigma)}}} \tag{9}$$

Equation 6 is a complex nonlinear equation that does not explicitly reveal the relationship between ellipticity and Poisson's ratio. Through numerical fitting, an empirical relationship with a correlation coefficient of 0.9775 was obtained[24]:

$$E = -0.4855\sigma + 0.797 \tag{10}$$

In Figure 1, α, β, and V_R are the P-wave, S-wave, and Rayleigh wave velocities, respectively. *Er* is the theoretical elliptical polarization ratio, and the solid line is the linear fit. As shown in Figure 1, with increasing Poisson's ratio, the elliptical polarization ratio decreases at a rate significantly faster than the rate of increase for the V_R/β ratio. This indicates that the elliptical polarization ratio is more sensitive to variations in Poisson's ratio. This equation clearly indicates an approximate inverse linear relationship between ellipticity and Poisson's ratio. This finding further substantiates the feasibility of using Rayleigh wave ellipticity for the evaluation of geological structures.

3. Numerical simulation

In this section, numerical simulations are employed to validate the response of Rayleigh wave ellipticity to changes in geological structure. Initially, a cuboid homogeneous medium model with dimensions of 600 m × 600 m × 400 m was constructed to simulate a homogeneous half-space. The medium properties were defined as follows: A density

of 2000 kg/m³, a P-wave velocity of 1000 m/s, and an S-wave velocity of 530 m/s. The model was discretized with a grid spacing of 2 m. In the simulation, a plane wave source was used to excite the Rayleigh wave field. The source wavelet was a 20 Hz Ricker wavelet. A linear array of 140 receivers was deployed along a central survey line with a receiver spacing of 2 m, and the data were sampled at a time interval of 0.0005 s. A schematic of the model is presented in Figure 2. For the homogeneous case, the entire model was assigned uniform properties. In contrast, for the heterogeneous simulation, a cavity was introduced and assigned a density of 1500 kg/m³, a P-wave velocity of 300 m/s, and an S-wave velocity of 150 m/s.

For a homogeneous medium with a density of 2000 kg/m³, a P-wave velocity of 1000 m/s, and an S-wave velocity of 530 m/s, the theoretical value of the Rayleigh wave ellipticity is 0.654. Figure 3A displays the simulated three-component seismic records obtained from this homogeneous medium model. In the simulation, a single linear source was employed to simulate Rayleigh surface waves in the far-field, and body waves were subsequently filtered out. As the Y-component is perpendicular to the direction of wave propagation, its amplitude is nearly zero in the homogeneous model. In contrast, both the vertical component (Z) and the component along the propagation direction (X) exhibit high amplitudes. Figure 3B presents the corresponding ellipticity profile, which clearly reflects the homogeneous characteristics of the medium. The calculated ellipticity is consistent with the theoretical value of 0.654. This demonstrates that in a homogeneous medium, the ellipticity of Rayleigh waves can effectively indicate the uniformity of the geological structure. Furthermore, by leveraging the relationship between ellipticity and Poisson's ratio, site characteristics can be determined.

Furthermore, a simulation was conducted for a heterogeneous medium containing a low-velocity cavity. The spherical low-velocity anomaly was characterized by a density of 1500 kg/m³, a P-wave velocity of 300 m/s, an S-wave velocity of 150 m/s, a diameter of 8 m, and its center was located at a depth of 16 m below the surface. Figure 4A presents the simulated three-component seismic records from this heterogeneous model, which also employed a single linear source to simulate far-field Rayleigh surface waves with body waves subsequently filtered. Similar to the homogeneous model, the amplitude of the Y-component, which is perpendicular to the propagation direction, is negligible, whereas the vertical (Z) and inline (X) components exhibit high amplitudes. Figure 4B shows the corresponding ellipticity profile. The regions outside the low-velocity anomaly clearly reflect the homogeneous
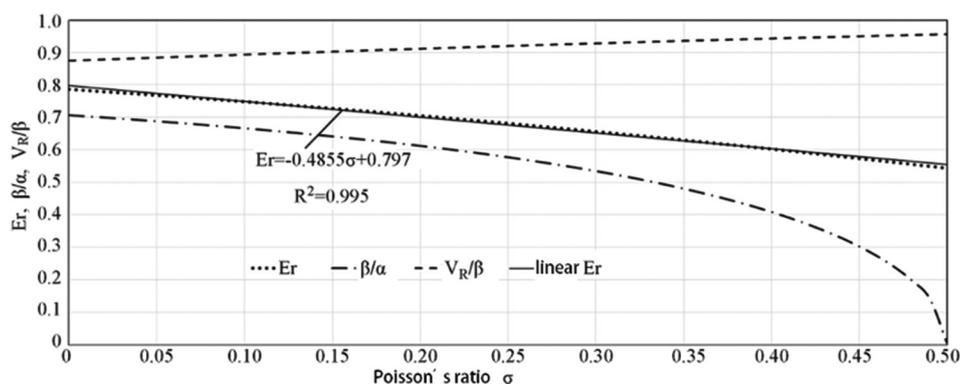
Figure 1. Approximate negative linear relationship between surface wave ellipticity and Poisson's ratio for a homogeneous half-space
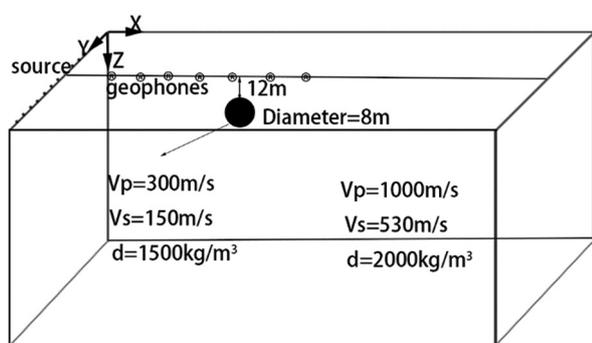

Figure 2. Numerical simulation model
Abbreviations: d: Density; V_p: P-wave velocity; V_s: S-wave velocity.

characteristics of the background medium. However, at an offset of approximately 170 m, a weak high-ellipticity anomaly and a strong low-ellipticity anomaly appear, which can be used to locate the low-velocity cavity. Notably, the anomaly imaged in the profile is displaced in the direction of wave propagation. This demonstrates that the Rayleigh wave ellipticity profile can effectively identify the location of localized geological anomalies.

The results from the two numerical simulations above indicate that the ellipticity of Rayleigh surface waves is sensitive to anomalies in the geological structure. By leveraging the established relationships between ellipticity, velocity, and Poisson's ratio, this method can effectively characterize the features of the geological structure. Consequently, it can serve as a valuable complement to the conventional site evaluation parameter, Vs30.

The application of the elliptical polarization ratio method in microtremor data processing fundamentally relies on the effective extraction of high-SNR Rayleigh waves. In this section, we investigate this extraction process by constructing a numerical model of microtremor signals. This model is developed by introducing random

noise and incorporating the propagation characteristics of multidirectional surface waves. The model is subsequently analyzed using techniques such as polarization analysis and directional filtering to isolate high-SNR Rayleigh waves.

To better simulate the physical characteristics of real-world microtremor signals, this study employed a homogeneous medium model with two oppositely oriented sources. The resulting synthetic seismogram contains various components, including multidirectional surface waves, P-waves, and boundary-reflected waves. On this basis, a microtremor dataset representing a complex interference environment was constructed by superimposing random noise with a maximum amplitude equal to 50% of the signal's maximum amplitude, as shown in Figure 5A. Figure 5B displays the record of coherently propagating Rayleigh waves, which was extracted after a series of processing steps, including high-amplitude signal screening, polarization analysis, and directional filtering.

Figure 6A illustrates the particle motion trajectories of the 25-trace synthetic microtremor record. Due to interference from noise, multidirectional Rayleigh waves, and body waves, the original record exhibits both linear and elliptical polarization phenomena, leading to significant disorder in the particle motion trajectories. In contrast, after optimization through methods such as event selection and polarization-based denoising, the extracted Rayleigh wave signal shows a significantly improved SNR, and its particle motion trajectories exhibit typical elliptical polarization characteristics (as shown in Figure 6B). These results confirm that the proposed technical scheme, which combines high-amplitude signal extraction with filtering, is feasible for isolating high-SNR Rayleigh waves from complex microtremor signals.
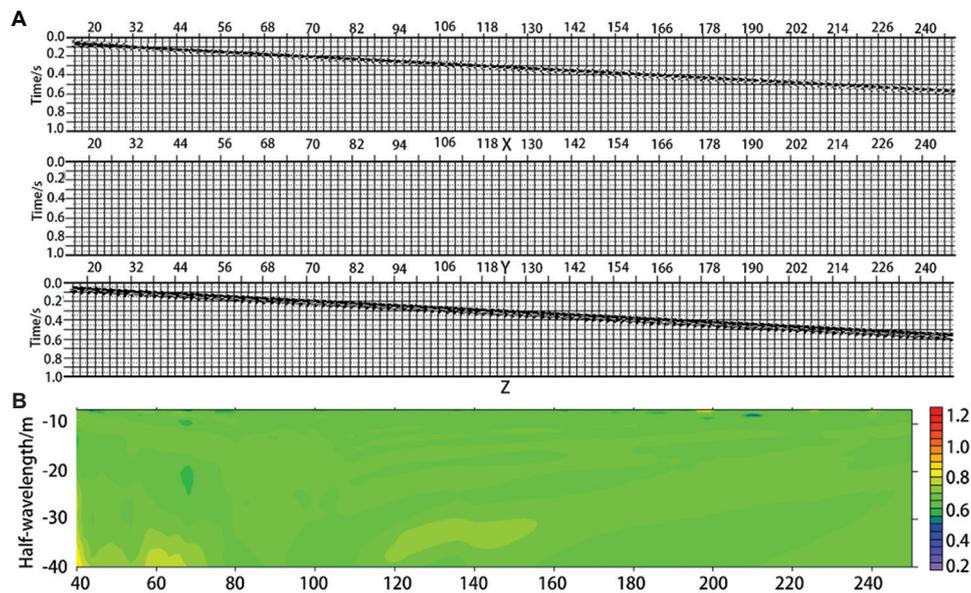
Figure 3. Seismic records and the corresponding ellipticity profile in a homogeneous half-space model, excited by a single plane source propagating along the main survey line. (A) Three-component seismic records along the central survey line, containing only a single set of Rayleigh surface waves. (B) The horizontal ellipticity profile at a depth of 0.5λ.
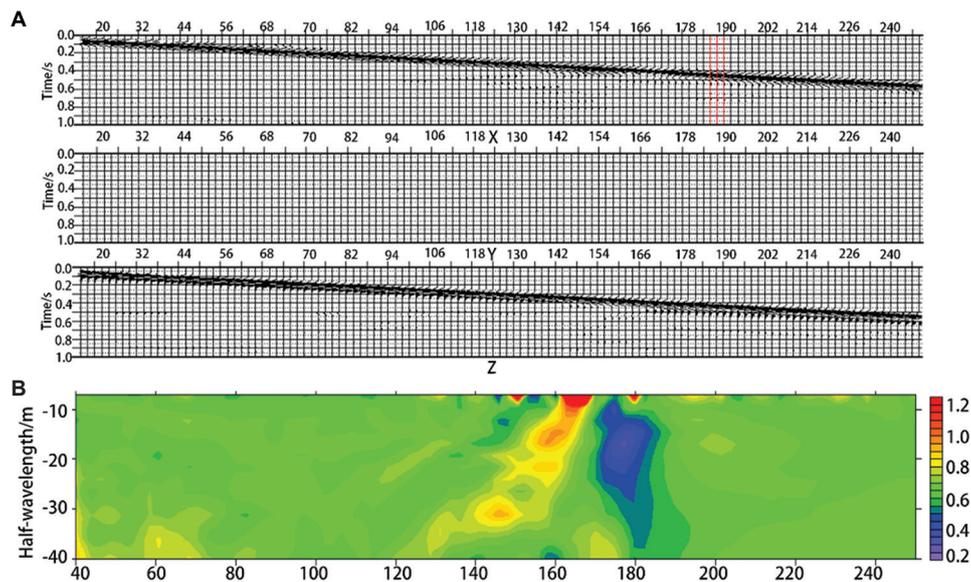
Figure 4. Seismic records and the corresponding ellipticity profiles in a heterogeneous half-space model, excited by a single plane source propagating along the main survey line. (A) Three-component seismic records along the central survey line contain only a single set of Rayleigh surface waves. (B) The horizontal ellipticity profile at a depth of 0.5λ, where λ is the dominant wavelength.

4. Data acquisition and analysis

To investigate the applicability of Rayleigh wave ellipticity from microtremor data for site evaluation and geological structure detection, this section focuses on three aspects: The acquisition of field data, the analysis of data characteristics, and the calculation of ellipticity profiles.

Furthermore, the accuracy of the results is validated through comparative analysis.

4.1. Materials

The stability of the ground is of paramount importance for all infrastructure, including buildings, high-speed railways, and highways. Consequently, site investigation
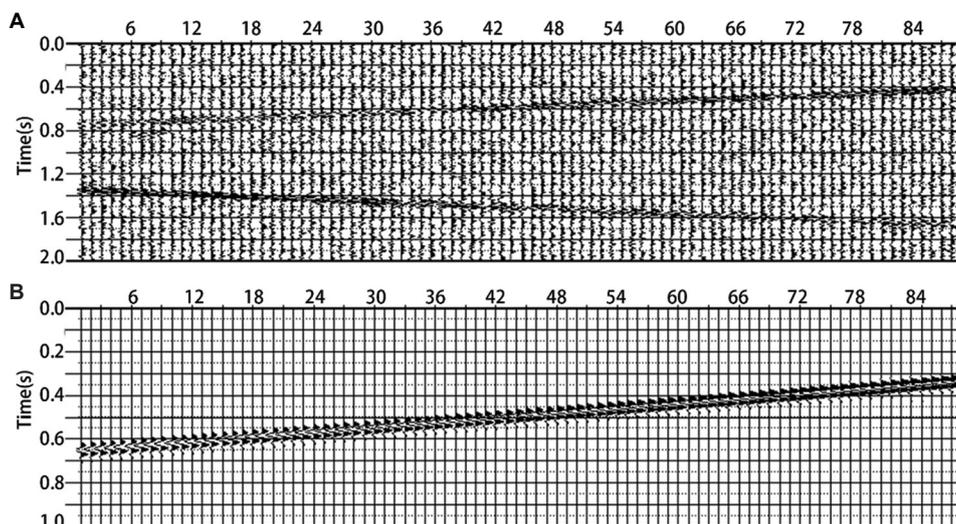
Figure 5. Vertical-component seismic records in a homogeneous medium. (A) Synthetic microtremor record. (B) Filtered Rayleigh wave record.
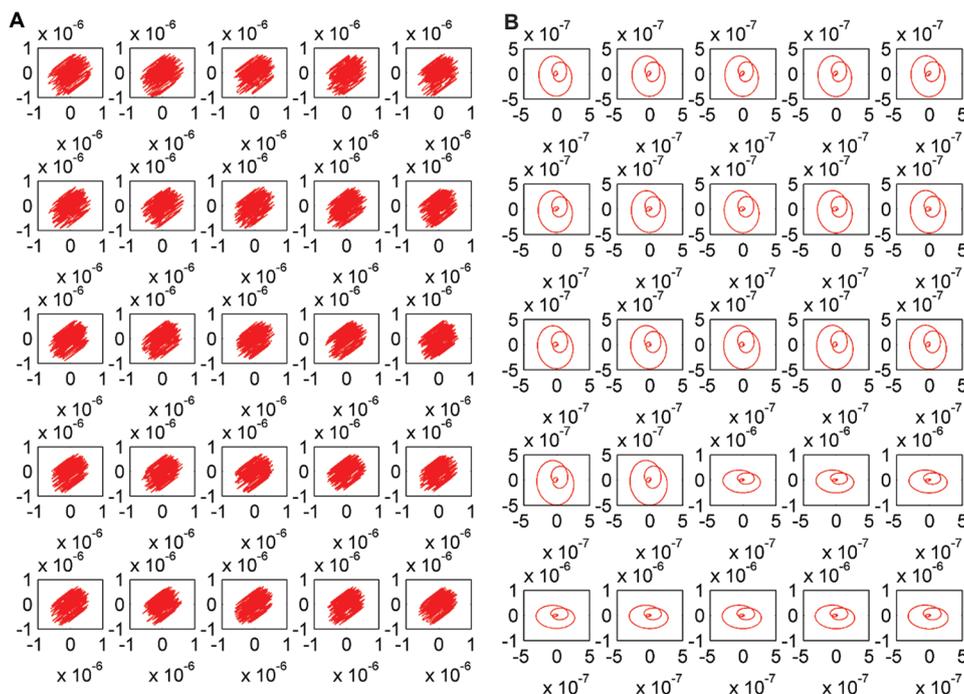

Figure 6. Particle motion trajectories of seismic records. (A) Trajectories of the synthetic microtremor record. (B) Trajectories of the Rayleigh wave record.

is an indispensable phase in construction engineering. To validate the practicality of the method proposed in this study, field data were used for verification. The case study data consist of microtremor records newly acquired along a survey line using three-component seismic instruments.

The data were collected in October 2015 at a construction site for a proposed railway line, with the objective of evaluating the stability of the geological structures along the route. The survey line was located in a mountainous area with elevations ranging from 350 m to 460 m. The site conditions were complex, featuring a varied surface of forests, shrubs, ponds, farmland, and residential houses, with some sections exhibiting steep topography. According to geological data, the bedrock in the area is primarily composed of mudstone, shale, and coal seams.

The geophones used for data acquisition had a frequency response range of 0.1–150 Hz. A total of 11 digital seismic instruments were deployed simultaneously

in an array along the survey line. The receiver spacing and sampling interval were set to 10 m and 0.01 s, respectively. The X-component was oriented along the survey line, the Y-component perpendicular to it, and the Z-component vertically. Considering the intensity of fieldwork and time constraints in the mountainous terrain, the recording duration for each setup was limited to 10 min. Over a 2-day period, a total of 12 setups were completed, yielding 132 three-component data traces. As the raw seismic records contained DC-offset interference, a band-pass filter from 0.1 Hz to 32 Hz was applied to the data. Figure 7A displays the gathering of the 132 vertical-component records, and Figure 7B shows the amplitude spectrum of the entire dataset.

The seismic records appear complex and chaotic, making it difficult to directly discern useful information. However, after applying amplitude gain, it is observed that some time segments exhibit relatively stable signals, whereas others are characterized by high-amplitude vibrational events. The amplitude spectrum of the 10-min records reveals that the signal energy is predominantly concentrated below 8 Hz. In contrast, the high-frequency components tend to exhibit characteristics consistent with white noise.

4.2. Field data analysis

This section analyzes the field microseismic signals in terms of their energy distribution, events with a high SNR, and the propagation direction of Rayleigh waves. This analysis serves as a preparatory step for the field data processing required by the microseism-based Rayleigh wave ellipticity method.

Initially, a single three-component seismic record with a duration of 600 s was selected. The microtremor signal was amplified using Geogiga Seismic Pro software (Geogiga

Technology Corp, Canada), and based on the observed amplitude distribution, two 10-s segments were extracted, as shown in Figure 8A and B. The segment in Figure 8A contains a distinct high-amplitude event, whereas the segment in Figure 8B is relatively stable, lacking any significant vibrational activity.

Time-frequency analysis was employed to characterize the signals in Figure 8A and B, with the resulting time-frequency distributions shown in Figure 9A and B, respectively. As shown in Figure 9A, the high-amplitude event occurring between 6 and 8 s in Figure 5A is composed of a low-frequency component at approximately 3 Hz and a high-frequency component at approximately 20 Hz. In contrast, the time-frequency plot in Figure 9B indicates that the energy is distributed nearly uniformly across both time and frequency, exhibiting stationary characteristics similar to those of white noise.

Conventional methods, such as the spatial autocorrelation and traditional ellipticity approaches, presuppose that seismic records adhere to the properties of a stationary random process. Consequently, strong vibrational events, such as the one depicted in Figure 8A, can severely compromise the final interpretation. In contrast, the present study seeks to extract geological information directly from such high-amplitude events, provided they are dominated by Rayleigh surface waves. The presence of these events in the microtremor records thus provides the fundamental basis for our methodology.

The subsequent analysis focuses on the characteristics of high-SNR events within the microtremor data. An SNR threshold is first established based on data quality, from which high-SNR events, each with a duration of 10 s (determined by site conditions and target depth), are extracted from the 600-s records at each station. A variable
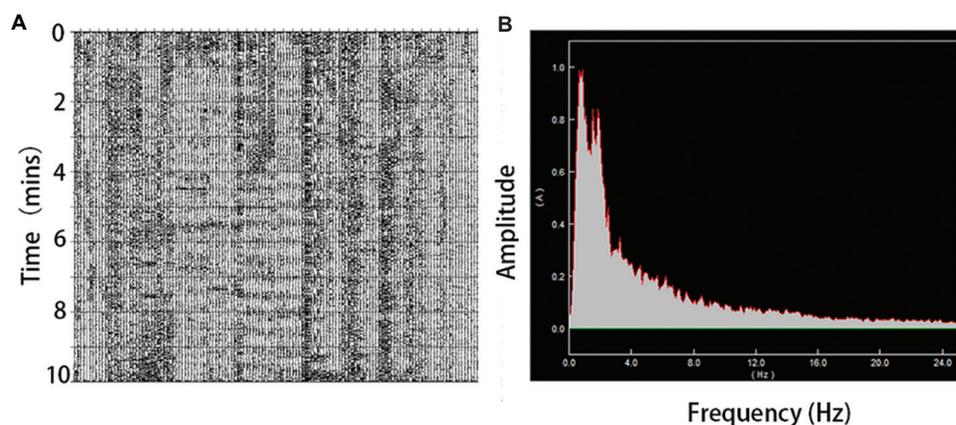
Figure 7. Seismic records and their corresponding amplitude spectrum. (A) The vertical-component seismic records from 132 channels, each with a 10-min duration. (B) The amplitude spectrum corresponding to (A).
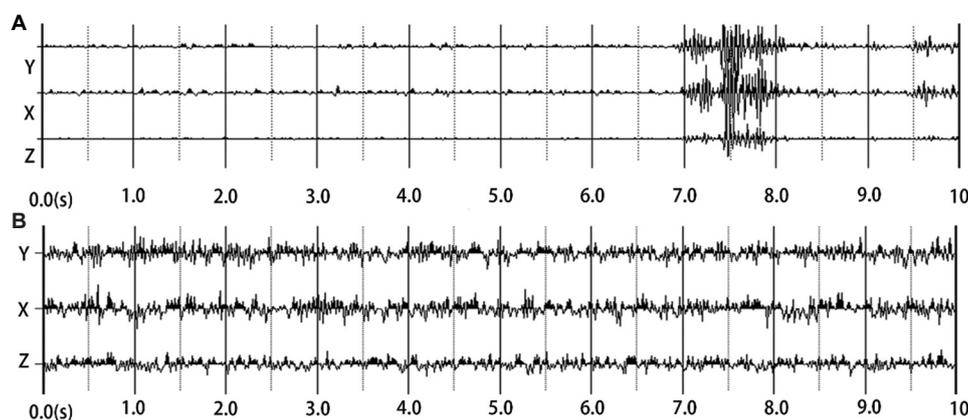
Figure 8. Three-component seismic records, where X, Y, and Z denote the two horizontal and vertical components, respectively. Panels (A) and (B) are microtremor records extracted from the 10-min, three-component seismic data after band-pass filtering from 0.1 Hz to 30 Hz.
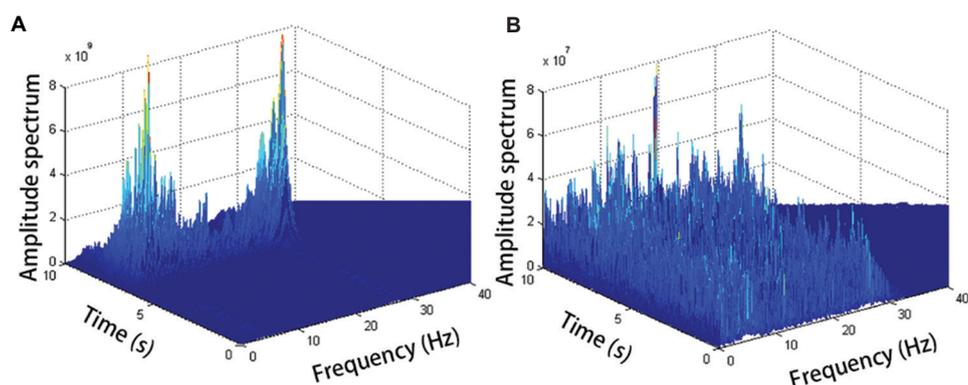
Figure 9. Time-frequency spectra. Panels (A) and (B) show the spectra for vertical component records containing a high-signal-to-noise ratio event and for those without, respectively.

number of such events, resembling those in Figure 8A, are identified at each location. If a station fails to produce an event meeting the initial criterion, the SNR threshold is incrementally lowered, or an estimation is performed using data from adjacent stations. It is important to note that the selected high-amplitude signals may originate from either Rayleigh surface waves or linearly polarized body waves.

Following the selection of high-SNR events, it is necessary to discriminate between signals dominated by Rayleigh waves and those dominated by linearly polarized waves. Phase-difference filtering is applied to all selected high-SNR events to isolate the former, with the objective of identifying at least one Rayleigh wave event for each of the 132 stations. It is crucial to note that this filtering step serves exclusively as a screening mechanism and is not part of the final signal processing for analysis.

Figure 10 displays the particle motion trajectories for 20 of the selected Rayleigh wave-dominated records. Although these signals are primarily composed of Rayleigh waves, they still contain high-frequency interference outside the

target band and residual linearly polarized waves. As a result, the trajectories exhibit an overall elliptical shape but are chaotic and lack a clear, well-defined geometry. Direct determination of the propagation direction from such raw trajectories would be significantly compromised by this interference, and accurate calculation of the ellipticity would be infeasible.

Time-frequency analysis is a standard technique for the investigation of microtremor signals, as it facilitates the clear discrimination of the principal components within a seismic record. Therefore, in this study, we applied time-frequency analysis to all Rayleigh wave-dominated records to identify the principal component of the signal, which is defined as the frequency, f_0, at which the energy is maximal. Subsequently, a band-pass filter centered at this f_0 is applied to the data. The particle motion trajectories of the processed microtremor records are presented in Figure 11.

As illustrated by the contrast between Figure 11 and the pre-filtered Figure 10, the filtering process yields distinctly elliptical particle motion trajectories, thereby
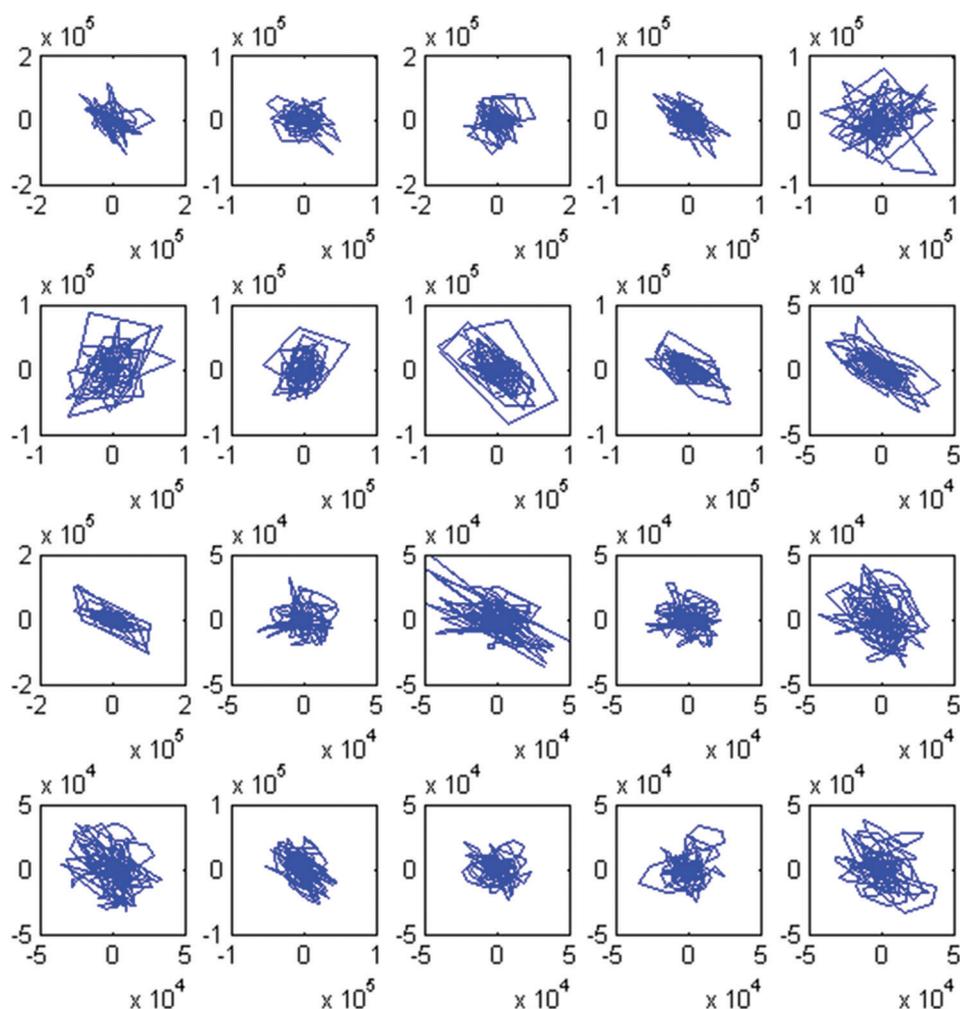
Figure 10. Particle motion trajectories for 20 of the selected Rayleigh wave-dominated records

confirming the dominance of Rayleigh wave components and their inherent elliptical polarization. This enables the subsequent identification of the propagation direction from the principal component of these filtered signals.

Given that numerical simulations show anomalies in polarization profiles shift along the propagation path, selecting codirectional Rayleigh waves is crucial for accurate polarization analysis. Consequently, a comprehensive directional analysis was performed on all Rayleigh wave-dominated data from the 132 geophones to identify a set of 132 high-SNR waves propagating uniformly. The 360° azimuthal range was partitioned into six 60° sectors, with the survey line oriented at 0°. Statistical results, exemplified by the 20 randomly selected geophone plots in Figure 12, reveal that most signal groups possess two to three dominant propagation directions, whereas some records exhibit a more uniform directional distribution. A notable

similarity was also observed in the directional statistics among the eleven concurrently acquired data sets.

In addition, a statistical analysis of the propagation directions of all high-SNR Rayleigh wave events was conducted across all stations. From the 132 datasets, each with a 10-min recording duration, a total of 6600 events were identified. The resulting azimuthal distribution is presented in Figure 13.

As shown in Figure 13, the number of events in the 0°–30° and 270°–360° sectors is slightly lower compared to other directions, although the overall distribution remains relatively uniform. This suggests that the high-SNR Rayleigh waves in this region do not fully satisfy the assumption of spatial stationarity. Concurrently, the presence of Rayleigh waves from various propagation directions within the signals makes it feasible to select a subset of codirectional waves for analysis.
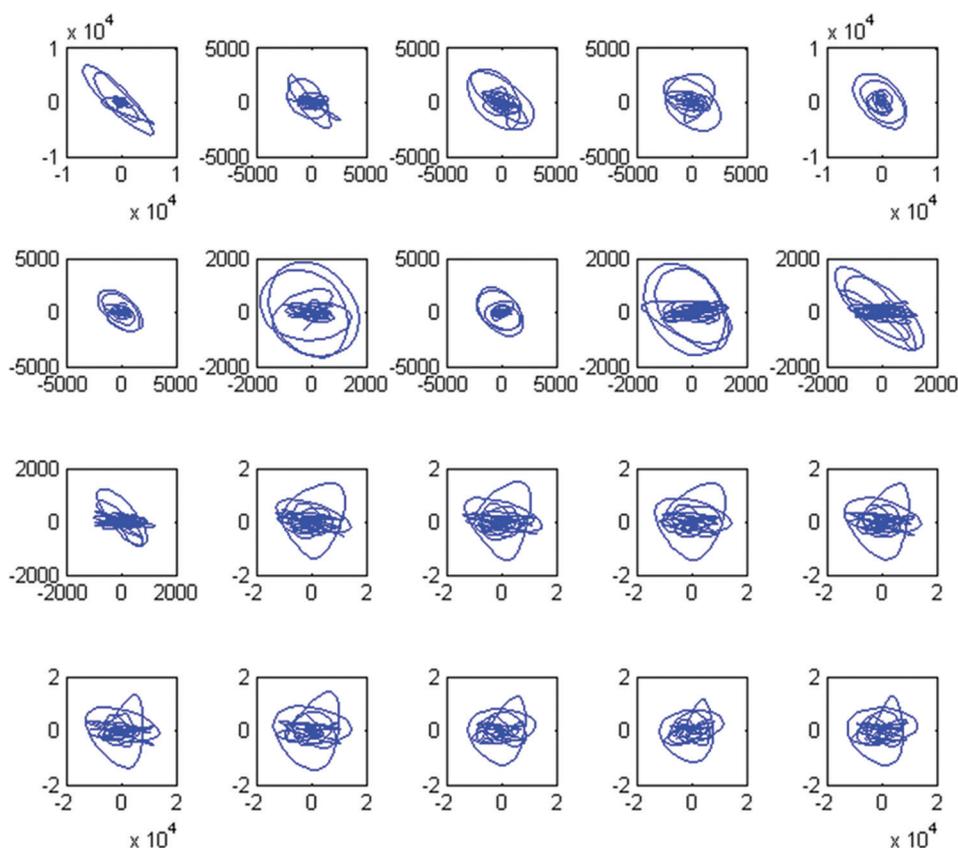
Figure 11. Particle motion trajectories of 20 Rayleigh wave-dominated microtremor records after principal frequency-centered band-pass filtering

In summary, the selection of high-SNR, codirectional Rayleigh waves from the *in situ* microtremor data is demonstrated to be a practical and feasible approach. Based on the results from both the overall and single-record directional statistics, the Rayleigh waves propagating in the direction opposite to the survey line were selected for the subsequent calculation of ellipticity. The analysis of the processed results is presented in the following section.

4.3. Data processing and analysis of results

Based on prior theoretical and numerical analyses, factors such as noise, linearly polarized waves, and multidirectional Rayleigh waves adversely affect the accuracy of ellipticity estimation. To address these issues in the field data, a six-step processing scheme was implemented: (1) band-pass filtering, (2) high-SNR event filtering, (3) phase-difference filtering, (4) directional filtering, (5) polarization filtering, and (6) ellipticity estimation.

This procedure successfully isolated 132 codirectional, high-SNR events dominated by Rayleigh waves. With the propagation direction known, the three-component data for these events were rotated to obtain the horizontal radial and vertical components. Figure 14 illustrates the phase relationship between these two components for a representative 4-s segment from 20 selected events, where the red and blue curves denote the vertical and radial components, respectively. A distinct phase difference at the peaks is evident for all signals, which validates that the selected events are indeed Rayleigh wave-dominant.

4.4. An ellipticity stacking methodology

The selection of high-SNR Rayleigh waves inherently allows for minor directional deviations, introducing stochastic errors into the processing results. While continuous microtremor records contain multiple such events that can be used to suppress these errors, conventional multitrace stacking is not feasible. This is because ellipticity dispersion is calculated from single-point, three-component data and is highly sensitive to propagation direction, as previously demonstrated.

To overcome this limitation, we developed a stacking and averaging method for ellipticity dispersion curves. Assuming a sufficiently long acquisition time, multiple suitable Rayleigh wave events can be identified at a given station. In this study, four sets of 132-trace, high-SNR, codirectional Rayleigh waves were extracted from 10-min
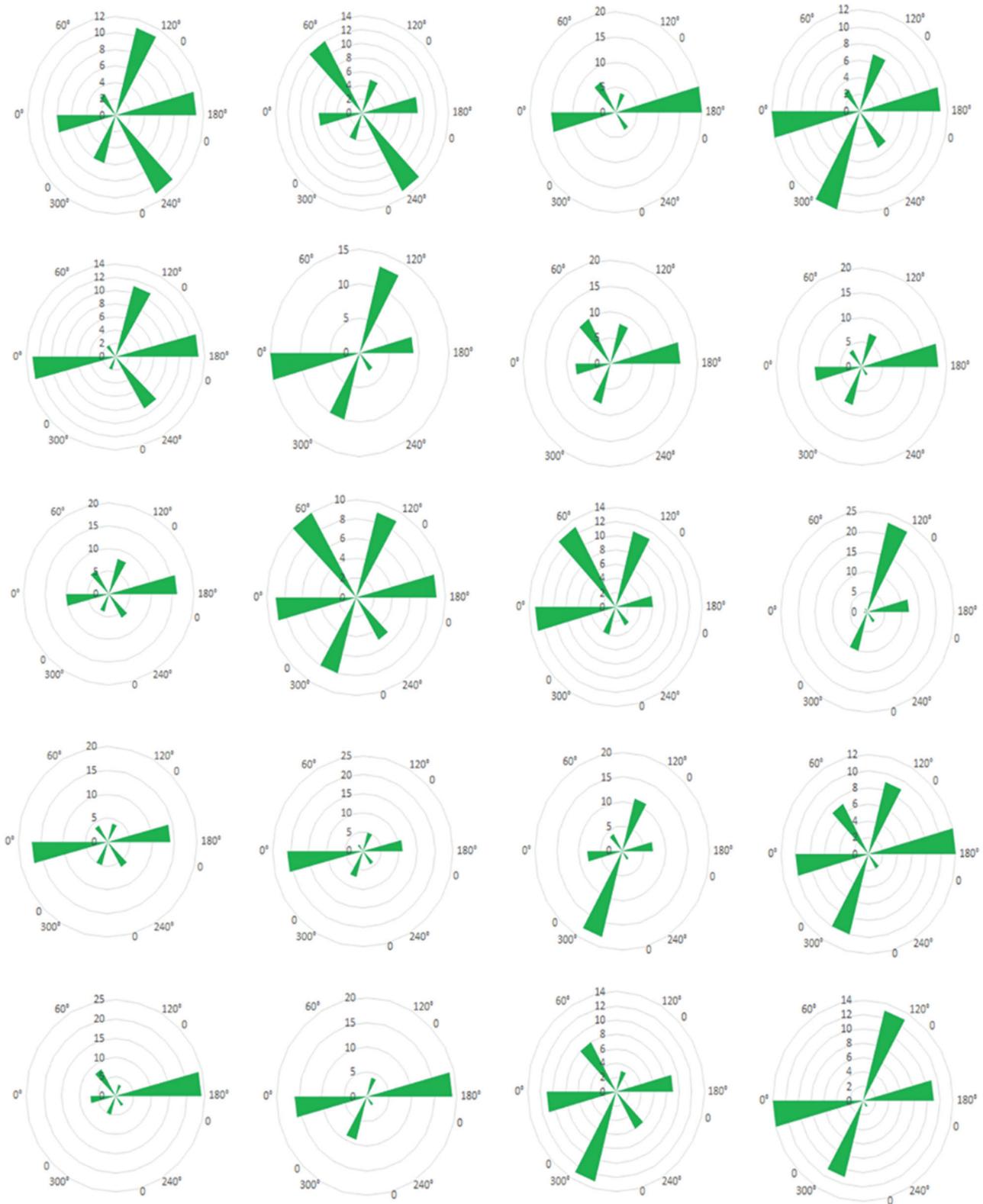
Figure 12. Rose diagrams of the azimuthal distribution of Rayleigh waves from data at 20 selected stations
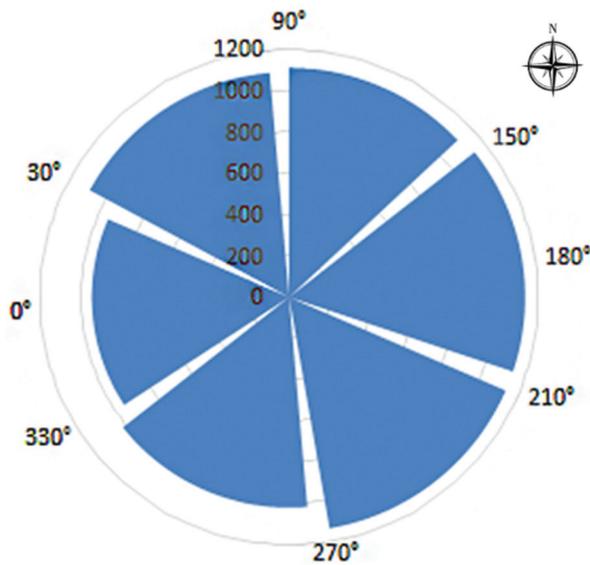
Figure 13. Rose diagram showing the azimuthal distribution of all Rayleigh wave events identified from the microtremor records

records. Their individual ellipticity dispersion curves were computed and then stacked to form composite profiles (Figure 15).

The four resulting profiles (Figure 15A-D) all successfully identify the low-ellipticity anomaly associated with the mined-out void at station 92100, as well as those at the fractured zones (stations 92600 and 93200). However, localized discrepancies are evident. The anomaly in Figure 15B at station 9280 is an artifact of low-frequency interference. The spurious anomaly near station 93200 in Figure 15C is inconsistent with the geological model, obscuring the fractured zone's extent. Figure 15D, while showing the major anomalies, lacks resolution in shallow structures and exhibits extremely low-ellipticity values at depth near stations 92100 and 93200. These localized artifacts, induced by data-related random errors, compromise the overall precision of the interpretation.

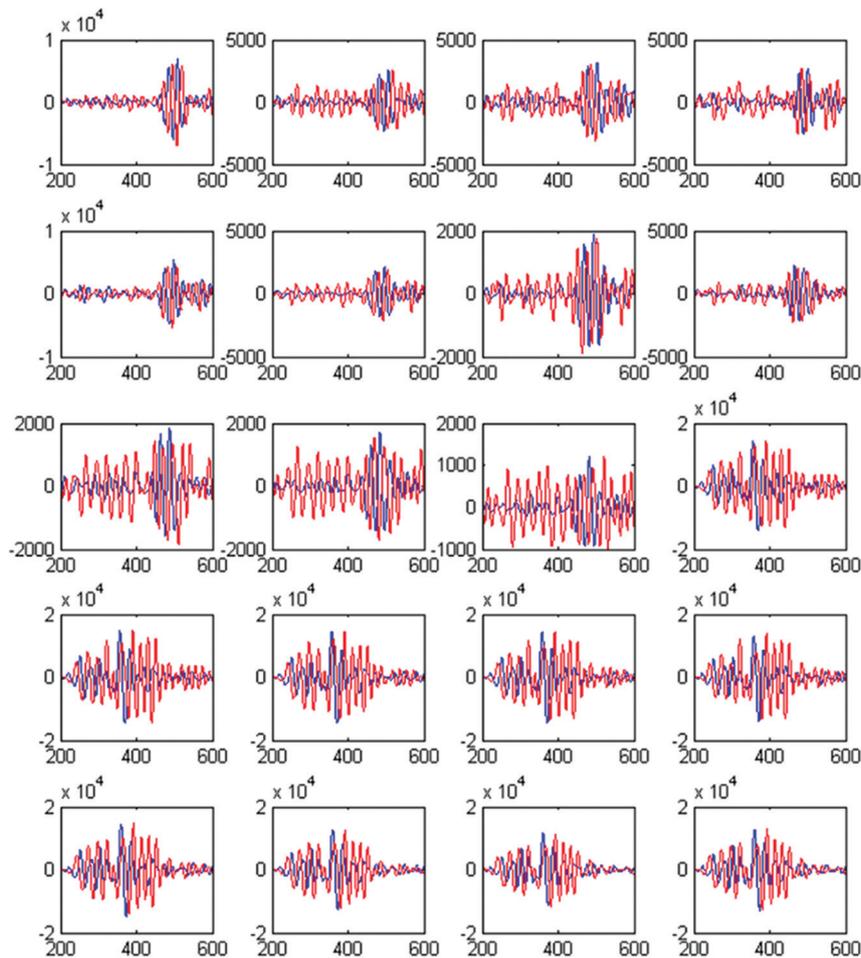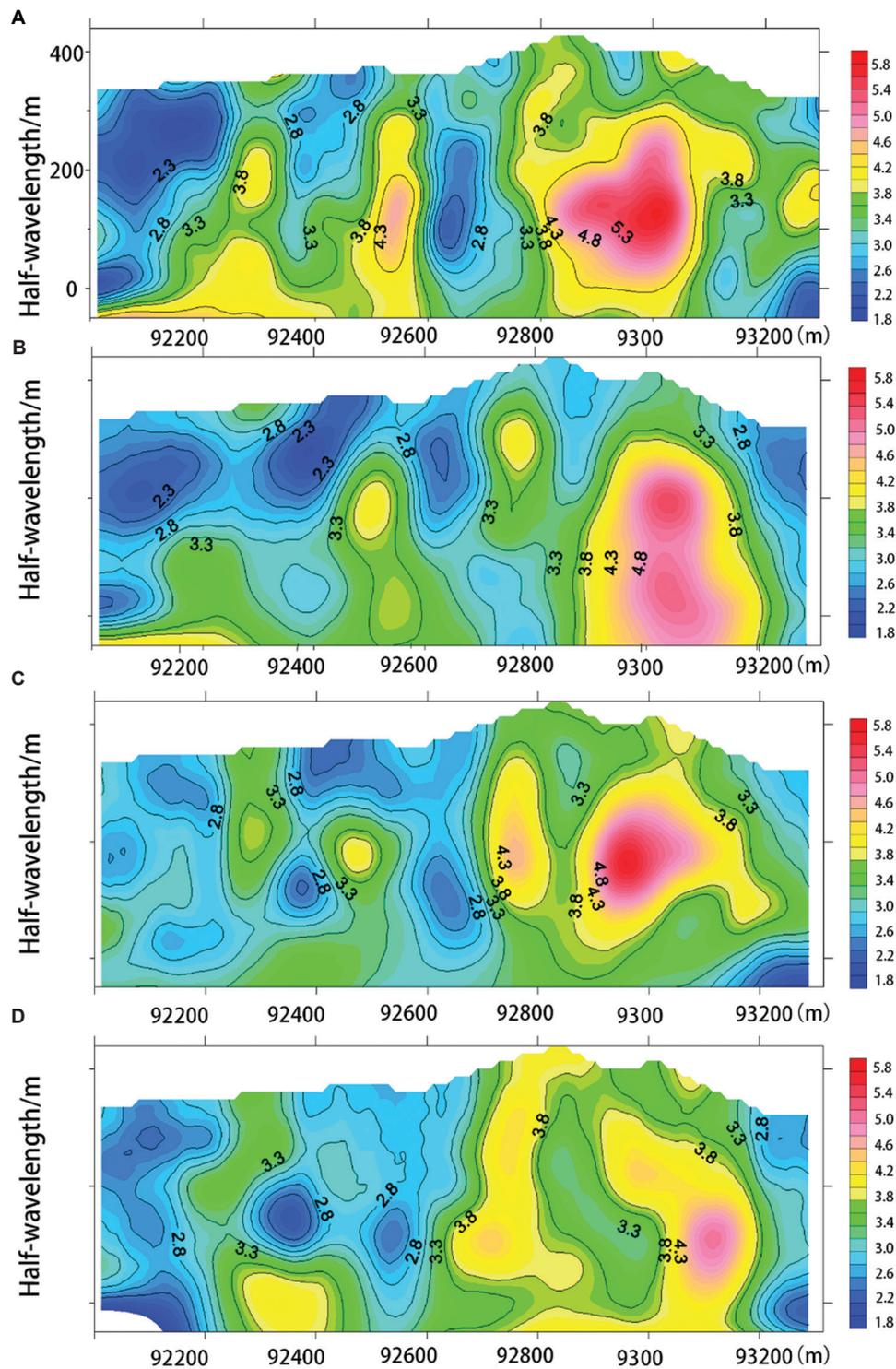In this study, the ellipticity was calculated for the four selected Rayleigh wave events from each station. By

Figure 14. Vertical and horizontal components of seismic records for 20 Rayleigh wave events

Figure 15. Ellipticity dispersion profiles from four individual Rayleigh wave events. (A-D) Results from a single, codirectional, high-SNR event at each station.
Abbreviation: SNR: Signal-to-noise ratio.

applying the stacking principle, the average of these four ellipticity values was computed to generate a mean ellipticity

dispersion profile, as shown in Figure 16A. A comparison between Figure 16A and B reveals a distinct low-ellipticity
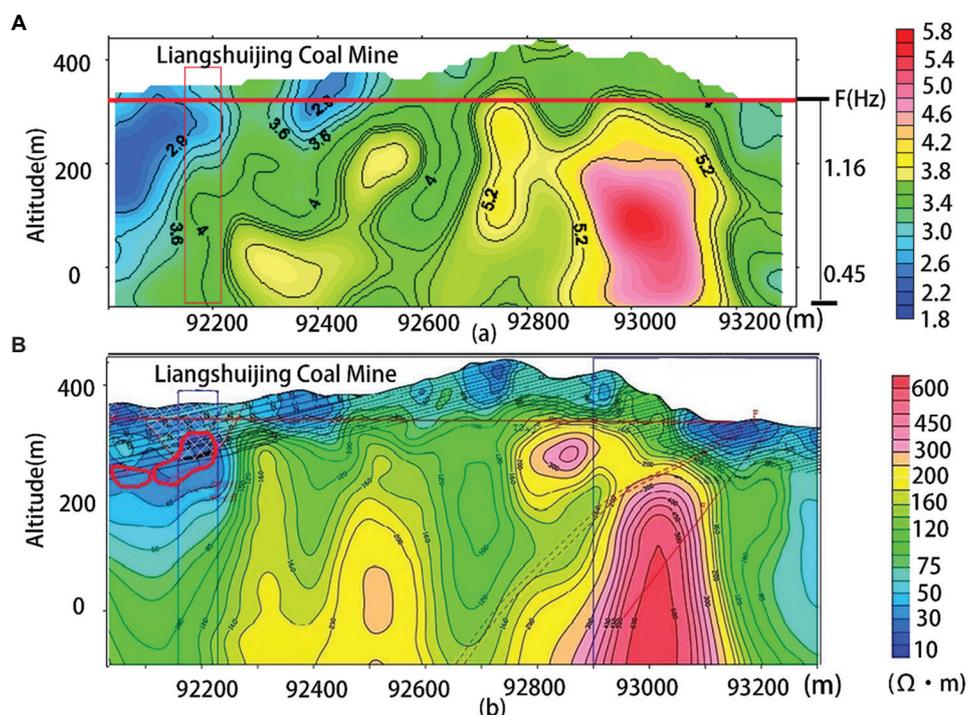
Figure 16. Ellipticity profiles calculated through various processing steps and the resistivity profile obtained from the magnetotelluric method. (A) Ellipticity dispersion profile of microtremor Rayleigh waves propagating along the survey line. (B) Resistivity cross-section derived from the magnetotelluric method.

anomaly at the location of the coal goaf before station 92200. Relative to the profiles in Figure 15A-D, the high-ellipticity anomaly between stations 92800–93200 and the fractured zone after station 93200 in Figure 16A exhibit a better correlation with the magnetotelluric data in detail. Notably, the ellipticity at a half-wavelength depth of 0 m is more physically reasonable. This indicates that stacking multiple events can produce a more accurate representation of the stratigraphic structure in the ellipticity profile. However, in the near-surface range of several tens of meters, its correspondence with the magnetotelluric data is less precise than that of Figure 16B. This is attributed to the fact that the 10-min dataset was insufficient to strictly select multiple codirectional Rayleigh wave events. Consequently, the selection criteria for the latter three events were relaxed in terms of SNR, which had a more significant impact on the high-frequency components. With a longer acquisition duration, the shallow part of the stacked profile could also achieve higher precision.

To further validate the practical applicability of the proposed method for site assessment and near-surface structural exploration, the results from the magnetotelluric survey along the same line were used as a benchmark. As shown in Figure 16, panel (a) presents the ellipticity dispersion profile of microtremor Rayleigh waves obtained via the aforementioned method, while panel (b) displays

the resistivity profile from the magnetotelluric survey. A comparative analysis of the two profiles reveals that at chainages 92150, 92700, and 92300, the distribution of high and low ellipticity anomalies is in strong agreement with the distribution of high and low resistivity. Given that the high and low values of both ellipticity and resistivity anomalies are closely correlated with high and low Poisson's ratios, respectively, this correspondence demonstrates the feasibility of applying the ellipticity method to engineering exploration. The region delineated by the red line in Figure 16B, representing a coal mine goaf, corresponds to a distinct low-ellipticity anomaly in Figure 16A.

5. Conclusion

First, this study theoretically analyzed the feasibility of utilizing Rayleigh wave ellipticity for site characterization and demonstrated its effectiveness in exploring both homogeneous and heterogeneous geological features through numerical simulations. The results indicate that in the absence of noise, Rayleigh wave ellipticity can clearly identify local anomalies within the geological structure.

Second, based on field data, a method for extracting high-SNR Rayleigh waves from microtremor signals was investigated. A macroscopic analysis of the entire dataset revealed that within each 10-min record, several high-amplitude seismic pulses occur randomly, whereas the

remaining segments exhibit characteristics approaching white noise. The presence of these high-amplitude pulses provides the foundation for the proposed method. A comparison between the original particle motion trajectories of 20 selected Rayleigh wave–dominated events and those filtered at the principal frequency revealed that, despite the presence of various interfering factors, the principal component of the selected signals is indeed the Rayleigh wave. Subsequently, a directional analysis was performed on all selected Rayleigh waves to determine their primary source directions. The results indicate that the directional distribution of the waves is generally uniform, with a relatively lower incidence along the survey line direction. This confirms the feasibility of extracting codirectional, high-SNR Rayleigh waves from the microtremor data at this site.

Finally, the processed ellipticity profiles were analyzed. Through data processing steps, including interference wave separation and filtering, the influence of interfering factors—such as Rayleigh waves from different propagation directions, linearly polarized waves, and white noise in the microtremors—was mitigated. The final processed results were then compared with the resistivity profile from the magnetotelluric survey along the same line. The comparison shows that the ellipticity profile clearly delineates the coal mine goaf, fractured zones, and bedrock, exhibiting strong agreement with the magnetotelluric results. The anomalous lateral shift observed in the ellipticity profile is attributed to the propagation direction of Rayleigh waves, whereas the resistivity distribution lacks this feature due to the near-vertical incidence of electromagnetic waves. To suppress the influence of random noise, the ellipticity dispersion profiles from four selected codirectional Rayleigh wave events were stacked and averaged. While the stacked profile, like the individual profiles, clearly identifies anomalous structures such as the goaf, it demonstrates a superior consistency with the resistivity profile in terms of deep structural details. For the investigation of lateral heterogeneities, such as mine goafs in mountainous terrains, the microtremor-based Rayleigh wave ellipticity dispersion method demonstrates comparable feasibility and flexibility to the conventional magnetotelluric resistivity method.

Acknowledgments

Funding

Conflict of interest

The authors declare they have no competing interests.

Author contributions

Conceptualization: Qingling Du, Qian Xu
Formal analysis: Qingling Du, Shijie Liu
Investigation: Shijie Liu, Qingling Du, Nan Guo
Methodology: Qingling Du, Shuai Liu
Writing–original draft: Qingling Du
Writing–review & editing: Qian Xu, Nan Guo, Denghui Gao

Availability of data

Data are available from the corresponding author upon reasonable request.

References

1. Soupios PM, Georgakopoulos P, Papadopoulos N, *et al.* Use of engineering geophysics to investigate a site for a building foundation. *J Geophys Eng.* 2007;4(1):94-103.

   doi: 10.1088/1742-2132/4/1/011

2. Rodgers MB, McVay MC, Horhota DJ, Hernando J, Paris JM. Operational limits of measuring while drilling in Florida limestone for geotechnical site characterization. *J Geotech Geoenviron Eng.* 2021;147(12):04021154.

   doi: 10.1061/(asce)gt.1943-5606.0002688

3. Wei X, Liu Y, Li X, Lu Y. Application of high density resistivity method in karst exploration: A case study. *Tehnički Vjesnik.* 2023;30(4):1283-1291.

   doi: 10.17559/tv-20230205000322

4. Lei X, Zhang J, Jin W, Han C, Xu X. The application of ambient noise and reflection seismic exploration in an Urban active fault survey. *Interpretation.* 2020;8(4):SU1-SU10.

   doi: 10.1190/int-2020-0085.1

5. Kachaje O, Yan L, Zhang Z. A Bayesian inference approach to reduce uncertainty in magnetotelluric inversion: A synthetic case study. *J Geosci Environ Prot.* 2019;7(2):62-75.

   doi: 10.4236/gep.2019.72005

6. Xia J, Miller RD, Park CB, Hunter JA, Harris JB, Ivanov J. Comparing shear-wave velocity profiles inverted from multichannel surface wave with borehole

measurements. *Soil Dyn Earthq Eng*. 2002;22(3):181-190.

doi: 10.1016/s0267-7261(02)00008-8

7. Park CB, Miller RD, Xia JH. Multichannel analysis of surface waves. *Geophysics*. 1999;64(3):800-808.

    doi: 10.1190/1.1444590

8. Xia JH, Miller RD, Park CB. Estimation of near-surface shear-wave velocity by inversion of Rayleigh waves. *Geophysics*. 1999;64(3):691-700.

    doi: 10.1190/1.1444578

9. Yu C, Wang Z, Tang M. Application of microtremor survey technology in a coal mine goaf. *Appl Sci*. 2023;13:466.

    doi: 10.3390/app13010466

10. Aki K. Space and time spectra of stationary stochastic waves, with special reference to microtremors. *Bull Earthq Res Inst*. 1957;35:415-456.

11. Capon J. High-resolution frequency-wavenumber spectrum analysis. *Proc IEEE*. 1969;57:1408-1418.

    doi: 10.1109/proc.1969.7278

12. Asten MW, Henstridge JD. Arrays estimators and use of microseisms for reconnaissance of sedimentary basins. *Geophysics*. 1984;48:1828-1837.

    doi: 10.1190/1.1441596

13. Horike M. Inversion of Phase velocity of long-period microtremors to the S-wave-velocity structure down to the basement in urbanized area. *J Phys Earth*. 1985;33:59-96.

    doi: 10.4294/jpe1952.33.59

14. Pan YD, Gao LL, Shigapov R. Multi-objective waveform inversion of shallow seismic wavefields. *Geophys J Int*. 2020;220:1619-1631.

    doi: 10.1093/gji/ggz539

15. Qingling D, Jianjun F, Yan Y, Kuanyao Z, Qian H. Application of near surface engineering defect exploration technology based on spatial autocorrelation. *Episodes J Int Geosci*. 2025;48(2):145-153.

    doi: 10.18814/epiiugs/2024/024022

16. Nogoshi M, Igarashi T. On the amplitude characteristics of microtremor (part 2). *Zisin J Seismol Soc Japan 2nd ser*. 1971;24:26-40.

    doi: 10.4294/zisin1948.24.1_26

17. Arai H, Tokimatsu K. S-wave velocity profiling by joint inversion of microtremor dispersion curve and horizontal-to-vertical (H/V) spectrum. *Bull Seismol Soc Am*. 2005;95(5):1766-1778.

    doi: 10.1785/0120040243

18. Woodhouse JH. Surface waves in a laterally varying layered structure. *Geophys J Int*. 1974;37(3):461-490.

19. Haney MM, Mikesell TD, Wijk KV, Nakahara H. Extension of the spatial autocorrelation (SPAC) method to mixed-component correlations of surface waves. *Geophys J Int*. 2012;91(1):189-206.

    doi: 10.1111/j.1365-246x.2012.05597.x

20. Maupin V. 3-D sensitivity kernels of the Rayleigh wave ellipticity. *Geophys J Int*. 2017;211(1):107-119.

    doi: 10.1093/gji/ggx294

21. Berbellini A, Schimmel M. Ferreira AM, Morelli A. Constraining S-wave velocity using Rayleigh wave ellipticity from polarization analysis of seismic noise. *Geophys J Int*. 2019;216(3):1817-1830.

    doi: 10.1093/gji/ggy512

22. Tokimatsu K, Miyadera Y. Characteristics of Rayleigh waves in microtremors and their relation to underground structures. *J Struct Constr Eng*. 1992;30:439.

23. Fäh D, Kind F, Giardini D. Inversion of local S-wave velocity structures from average H/V ratios, and their use for the estimation of site-effects. *J Seismol*. 2003;7(4):449-467.

    doi: 10.1023/b: jose.0000005712.86058.42

24. Yu W, Liu Z. A numerical study of the Rayleigh wave particle motions excited by a point source and Poisson's ratio for lateral inhomogeneous half-spaces. *J Appl Geophys*. 2015;123:242-255.

25. Tran TT, Vinh PC, Ohrnberger M, Malischewsky P, Aoudia A. An improved formula of fundamental resonance frequency of a layered half-space model used in H/V ratio technique. *Pure Appl Geophys*. 2016;173:2803-2812.

    doi: 10.1007/s00024-016-1313-0

26. Bignardi S. The uncertainty of estimating the thickness of soft sediments with the HVSR method: A computational point of view on weak lateral variations. *J Appl Geophys*. 2017;145:28-38.

    doi: 10.1016/j.jappgeo.2017.07.017

27. Picotti S, Francese R, Giorgi M, Pettenati F, Carcione JM. Estimation of glacier thicknesses and basal properties using the horizontal-to-vertical component spectral ratio (HVSR) technique from passive seismic data. *J Glaciol*. 2017;63(238):229-248.

    doi: 10.1017/jog.2016.135

28. Abu Zeid N, Corradini E, Bignardi S, Nizzo V, Santarato G. The passive seismic technique "HVSR" as a reconnaissance tool for mapping paleo-soils: The case of the pilastri archaeological site, Northern Italy. *Archaeol Prospect*. 2017;24(3):245-258.

    doi: 10.1002/arp.1568

29. Fäh D, Kind F, Giardini D. A theoretical investigation

doi: 10.1111/j.1365-246X.1974.tb04098.x

of average H/V ratios. *Geophys J Int*. 2001;145(2): 535-549.

doi: 10.1046/j.0956-540x.2001.01406.x

30. Xu H, Yin X, Qi Q, Mi B, Sun S, Luo Y. Determination of near-surface shear-velocity structure based on the joint inversion of Rayleigh-wave dispersion and ellipticity from multistation active-seismic records. *Geophysics*. 2022;87(3):21-32.

doi: 10.1190/geo2021-0176.1

31. Du Q, Pan Y, Yan Y. Research and application of Rayleigh wave extraction method based on microtremors signal analysis. *Front Phys*. 2023;11:1158049.

doi: 10.3389/fphy.2023.1158049

32. Poggi V, Fäh D, Burjanek J, Giardini D. The use of Rayleigh-wave ellipticity for site-specific hazard assessment and microzonation: Application to the city of Lucerne, Switzerland. *Geophys J Int*. 2012;188(3):1154-1172.

doi: 10.1111/j.1365-246x.2011.05305.x